Effect of protein steric constraints on the symmetry of membrane protein polyhedra

Mingyuan Ma and Christoph A. Haselwandter

Department of Physics & Astronomy and Department of Biological Sciences, University of Southern California, Los Angeles, California 90089, USA

(Received 20 June 2020; accepted 4 October 2020; published 23 October 2020)

Experiments have shown that, in an aqueous environment, lipids and membrane proteins can self-assemble into membrane protein polyhedral nanoparticles (MPPNs). MPPNs are closed, spherical vesicles composed of a lipid bilayer membrane and membrane proteins, with a polyhedral arrangement of membrane proteins. The observed symmetry and size of MPPNs can be understood from the interplay of protein-induced lipid bilayer deformations in MPPNs, topological defects in protein packing necessitated by the spherical shape of MPPNs, and thermal fluctuations in MPPN self-assembly. We explore here the effect of protein steric constraints on MPPN shape. The protein steric constraints considered here may arise from a well-defined shape of protein domains outside the membrane, entropic repulsion between membrane proteins with flexible domains outside the membrane, or binding of other molecules to membrane proteins. Calculating MPPN self-assembly diagrams under protein steric constraints we find that protein steric constraints can strongly affect MPPN self-assembly. Depending on the specific scenario considered, protein steric constraints can leave large portions of the MPPN self-assembly diagrams with no clearly defined MPPN symmetry or substantially expand the regions of MPPN self-assembly diagrams dominated by highly symmetric MPPN states, such as MPPNs with icosahedral or snub cube symmetry. Our results suggest that modification of protein steric constraints may allow the directed self-assembly of MPPNs with specified symmetry, size, and protein composition and may thus facilitate the further utilization of MPPNs for membrane protein structural analysis or targeted drug delivery.

DOI: 10.1103/PhysRevE.102.042411

I. INTRODUCTION

Cell membranes are one of the fundamental hallmarks of life [1,2]. Cell membranes typically consist of a lipid bilayer, which self-assembles from lipids suspended in an aqueous environment, and membrane proteins, which reside in the lipid bilayer and regulate many physiological processes [3–5]. Experiments have demonstrated that if membrane proteins and suitably chosen lipids are mixed at a defined ratio in an aqueous environment, membrane proteins and lipids can self-assemble into membrane protein polyhedral nanoparticles (MPPNs) [6,7]. MPPNs are closed, spherical vesicles composed of a lipid bilayer membrane and membrane proteins, with a polyhedral arrangement of membrane proteins. In particular, it was observed [6,7] that mechanosensitive ion channels of small conductance (MscS) and diC14:0 lipids predominantly self-assemble into MPPNs composed of 24 MscS proteins, with each MscS protein being located at the vertex of a snub cube and a MPPN diameter of approximately 20 nm at the bilayer midplane. The closed surfaces of MPPNs can support transmembrane gradients mimicking the gradients in pH, voltage, or chemical composition typically found across cell membranes [6], while the regular polyhedral arrangement of membrane proteins in MPPNs could be utilized for structural studies of membrane proteins [8–10]. MPPNs have thus been proposed [6] as a strategy for the structural analysis of membrane proteins under physiologically relevant transmembrane gradients.

A mean-field model of MPPN self-assembly [11,12] successfully predicts the observed symmetry and size of MPPNs formed from MscS proteins [6,7]. In this mean-field model, the dominant symmetry and size of MPPNs emerge from the interplay of protein-induced lipid bilayer deformations in MPPNs, topological defects in protein packing necessitated by the spherical shape of MPPNs, and thermal fluctuations in MPPN self-assembly. Structural biology has shown, however, that membrane proteins often have large domains with well-defined shapes outside the membrane [1,13–15]. Such protein domains outside the membrane impose restrictions on the arrangement of membrane proteins in MPPNs and, hence, are expected to affect MPPN shape. We extend here the mean-field model of MPPN self-assembly [11,12] to explore the effect of protein steric constraints on MPPN shape. Examples of membrane proteins with large domains with well-defined shapes outside the membrane include some types of potassium channels, molecular machines such as ATP synthase, and, potentially, SARS-CoV-2 spike proteins [1,13–19]. Effective steric constraints on membrane protein separation in MPPNs may also arise through the binding of other molecules to membrane proteins or entropic protein repulsion due to large but flexible protein domains outside the membrane. In Sec. II we describe in detail the mean-field model of MPPN self-assembly employed here. Section III surveys the effect of protein steric constraints on MPPN self-assembly diagrams. Finally, in Sec. IV we provide a summary and conclusions of the work described in this article.

II. CALCULATION OF MPPN SELF-ASSEMBLY DIAGRAMS

Our calculations of MPPN self-assembly diagrams are based on the mean-field approach developed in Refs. [11,12]. The purpose of this section is to summarize this mean-field model of MPPN self-assembly and to describe how this model can be extended to account for protein steric constraints arising from protein domains outside the membrane. At the mean-field level, the observed MPPN symmetry and size [6,7] can be understood [11,12] by considering the interplay of thermal fluctuations in MPPN self-assembly, protein-induced lipid bilayer deformations in MPPNs, and topological defects in protein packing arising from the spherical shape of MPPNs. Sections II A–II D describe the resultant contributions to the MPPN energy. In Sec. II E we discuss how steric constraints enter the calculation of MPPN self-assembly diagrams. We note that the mean-field approach employed here is, in general, not expected to apply to situations in which MPPNs self-assemble from distinct membrane proteins with, for instance, heterogeneous size, in which case a more detailed molecular model of MPPN symmetry is required [20].

A. Thermal effects

To ascertain the role of thermal effects in MPPN self-assembly, we note [11,12] that MPPNs were obtained experimentally [6,7] in dilute, aqueous solutions with a protein number fraction,

$$c = \sum_n \frac{N_n}{N_w} \approx 7.8 \times 10^{-8} \ll 1, \tag{1}$$

where N_n denotes the total number of proteins bound in MPPNs with n proteins each and N_w denotes the total number of solvent molecules in the system. We take N_w to be dominated by contributions due to water. Furthermore, we take the temperature of the system, T, to be fixed. We assume that the system is in a thermodynamic equilibrium state minimizing the Helmholtz free energy, $F = U - TS$, where U and S are the internal energy and the entropy of the system, respectively.

In the dilute limit $c \ll 1$ with no interactions between MPPNs, U is given by [11,12]

$$U = N_w \sum_n \Phi(n) E_{\min}(n), \tag{2}$$

where the MPPN number fraction $\Phi(n) = N_n/nN_w$ and $E_{\min}(n)$ is the minimum MPPN energy, and S is given by the mixing entropy [21,22]

$$S = -N_w k_B \sum_n \Phi(n)[\ln \Phi(n) - 1], \tag{3}$$

where k_B is Boltzmann's constant. Minimization of F with respect to $\Phi(n)$ thus yields [11,12,21–23]

$$\Phi(n) = e^{[\mu n - E_{\min}(n)]/k_B T}, \tag{4}$$

where the protein chemical potential μ is determined by the constraint

$$\sum_n n\Phi(n) = c, \tag{5}$$

imposing a fixed protein number fraction in the system. We restrict n to the range $10 \leqslant n \leqslant 80$. For all the calculations described here we employ the protein number fraction c in Eq. (1) used in experiments on MPPNs formed from MscS proteins [6,7]. For given $E_{\min}(n)$, Eq. (5) thus fixes the protein chemical potential μ.

We represent MPPN self-assembly diagrams in terms of the MPPN equilibrium distribution,

$$\phi(n) = \frac{\Phi(n)}{\sum_{n=10}^{80} \Phi(n)}. \tag{6}$$

For given $E_{\min}(n)$, $\phi(n)$ is determined via Eqs. (4)–(6) with Eq. (1). We obtain $E_{\min}(n)$ by minimizing the MPPN energy $E(n, R)$, at each n, with respect to the MPPN radius at the bilayer midplane, R, subject to steric constraints arising from the finite size of lipids and proteins (see Secs. II B–II E). We write $E(n, R)$ as

$$E(n, R) = E_h(n, R) + E_u(n, R) + E_d(n, R), \tag{7}$$

where E_h, E_u, and E_d denote contributions to E due to lipid bilayer midplane deformations in MPPNs, protein-induced lipid bilayer thickness deformations in MPPNs, and topological defects in protein packing in MPPNs, respectively. Sections II B–II D provide a discussion of these contributions to E. In Sec. II E we discuss how steric constraints enter $E_{\min}(n)$ and summarize the numerical procedure for the calculation of $E_{\min}(n)$ employed here.

B. MPPN bilayer midplane deformations

Membrane proteins often produce elastic shape deformations of the surrounding lipid bilayer membrane [5,24–26]. These bilayer shape deformations, and their associated elastic energy, depend on the elastic properties of the lipid bilayer under consideration, key properties of the protein structure such as the bilayer-protein contact angle α and the protein hydrophobic thickness w [see Fig. 1(a)], and the supramolecular protein arrangement. Based on the molecular structure of MscS [11,27,28] we consider here MPPNs formed from (approximately) rotationally symmetric membrane proteins, for which protein-induced elastic bilayer deformations are expected to favor hexagonal protein arrangements [29–35]. The elastic energy of lipid bilayer deformations in MPPNs can then be estimated using a mean-field approach [11,12,29–31] in which the boundary of the hexagonal unit cell of the protein lattice is approximated by a circle. We thus divide the surface of MPPNs containing n proteins into n identical, circular membrane patches, each with a protein at its center.

We use here the Monge parametrization of surfaces, and denote the in-plane radial coordinate in the membrane patch by ρ [Fig. 1(a)]. We have $\rho_i \leqslant \rho \leqslant \rho_o$, where ρ_i is the protein radius in the bilayer midplane and the patch size $\rho_o(n, R) = R \sin\beta$, where β is the patch boundary angle mandated by the spherical shape of MPPNs [Fig. 1(a)]. Throughout this article we use the value $\rho_i = 3.2$ nm corresponding to closed-state MscS proteins [11,27,28]. We set $\beta = \arccos[(n-2)/n]$ [30] so that, for a spherical MPPN shape, the total area covered by membrane patches, $2n\pi R^2(1 - \cos\beta)$, is equal to the total MPPN area, $4\pi R^2$, at closest (hexagonal) protein packing. The spherical topology of MPPNs necessitates defects in this

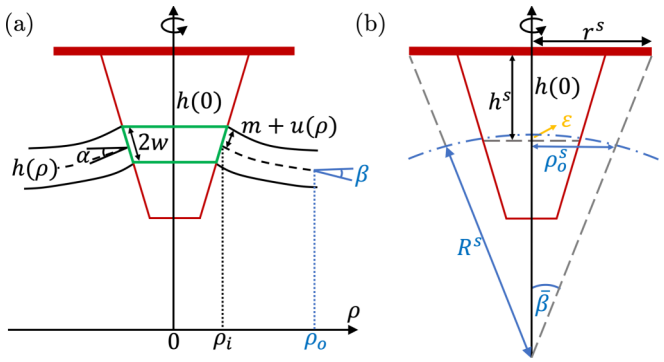

FIG. 1. Schematics of (a) protein-induced lipid bilayer deformations in MPPNs and (b) the geometry of MPPNs. We take each MPPN membrane patch to have a protein at its center at $\rho = 0$ and to be symmetric about the rotation axis $h(0)$. As indicated in panel (a), we denote the protein radius in the bilayer midplane by ρ_i, the MPPN membrane patch size by ρ_o, the height of the bilayer midplane by $h(\rho)$, and one-half the bilayer hydrophobic thickness by $u(\rho) + m$, where m is one-half the unperturbed bilayer thickness. As indicated in panel (b), we account for steric constraints on MPPN patch size due to protein domains outside the membrane through the in-plane protein radius outside the membrane r^s and the effective protein height h^s, which we define with respect to the protein hydrophobic midplane (dashed horizontal line). The protein height with respect to the MPPN center is given by $h^s + R - \epsilon$, where R is the MPPN radius and ϵ is an offset due to the finite protein size. The effective steric constraint on the membrane patch size in the bilayer midplane, ρ_o^s, depends on r^s and h^s. The schematic in panel (b) corresponds to the smallest R allowed by steric constraints due to protein domains outside the membrane, $R = R^s$, for which we have $R^s = \rho_o^s/\sin\bar{\beta}$ (see Sec. II E).

energetically preferred protein packing, which we return to in Sec. II D.

One key contribution to the MPPN energy in Eq. (7) arises due to bending deformations of the lipid bilayer midplane field $h(\rho)$ [Fig. 1(a)]. The energy cost associated with these lipid bilayer deformations is captured by the bilayer midplane deformation energy [4,36–38]

$$G_h = \frac{K_b}{2}\int dA\left(\nabla^2 h\right)^2, \tag{8}$$

where K_b is the lipid bilayer bending rigidity, the area element $dA = 2\pi\rho d\rho$ in polar coordinates, and ∇^2 is the Laplace operator in polar coordinates. For the diC14:0 lipids used for MPPNs formed from MscS proteins [6,7] we have $K_b \approx 14\ k_BT$ [39]. We set $K_b = 14\ k_BT$ throughout this article. We assume in Eq. (8), and throughout this article, that contributions to the MPPN energy due to lateral membrane tension can be neglected. Our analysis could be extended to allow for a nonzero membrane tension [12]. Furthermore, we assume throughout this article that the lipid bilayer membrane does not show a spontaneous curvature, and take the dominant bilayer shape to be the bilayer shape with lowest elastic energy.

The Euler-Lagrange equation associated with Eq. (8) is given by $\nabla^4 h = 0$, which has the general solution

$$h(\rho) = A_h\rho^2 + B_h + C_h\ln\rho + D_h\rho^2\ln\rho \tag{9}$$

for circular membrane patches with rotational symmetry about the protein center, where A_h, B_h, C_h, and D_h are constants to be determined by the boundary conditions at the bilayer-protein interface and at the outer boundary of the membrane patch. As indicated in Fig. 1(a), we take the slope at the bilayer-protein interface to be fixed by the bilayer-protein contact angle α,

$$h'(\rho_i) = -\tan\alpha \equiv a. \tag{10}$$

For reference, we note that for MscS we have $\alpha \approx 0.46$–0.54 rad [11,27,28]. The spherical geometry of MPPNs mandates that

$$h'(\rho_o) = -\tan\beta \equiv b. \tag{11}$$

We allow $h(\rho_o) - h(\rho_i)$ to be adjusted freely as part of the minimization procedure, which amounts to the natural boundary condition [30,40]

$$\frac{d}{d\rho}\nabla^2 h(\rho) = 0 \tag{12}$$

at $\rho = \rho_i$ or, equivalently, $\rho = \rho_o$. Noting that the choice of the reference point $h(\rho) = 0$ does not affect Eq. (8), substitution of the solution of the Euler-Lagrange equation for Eq. (8) [Eq. (9)] back into Eq. (8) [30] thus yields the MPPN midplane deformation energy,

$$E_h(n, R) = \frac{2n\pi K_b(b\rho_o - a\rho_i)^2}{\rho_o^2 - \rho_i^2}, \tag{13}$$

for n identical MPPN membrane patches.

C. MPPN bilayer thickness deformations

In addition to the bilayer midplane deformations considered in Sec. II B, membrane proteins typically deform the hydrophobic thickness of lipid bilayer membranes [5,24–26]. The corresponding elastic energy of membrane shape deformations in MPPNs [12] can be estimated from the bilayer thickness deformation energy [25,41,42]

$$G_u = \frac{1}{2}\int dA\left[K_b(\nabla^2 u)^2 + K_t\left(\frac{u}{m}\right)^2\right], \tag{14}$$

where $u(\rho)$ is the lipid bilayer thickness deformation field, m is one-half the unperturbed bilayer thickness [Fig. 1(a)], and K_t is the bilayer thickness deformation modulus. For the diC14:0 lipids used for MPPNs formed from MscS proteins [6,7] we have $m \approx 1.76$ nm and $K_t \approx 56.5\ k_BT/\text{nm}^2$ [39,43]. We set $m = 1.76$ nm and $K_t = 56.5\ k_BT/\text{nm}^2$ throughout this article. The Euler-Lagrange equation associated with Eq. (14) is given by

$$(\nabla^2 - \nu_+)(\nabla^2 - \nu_-)u = 0, \tag{15}$$

where

$$\nu_\pm = \pm\sqrt{-\frac{K_t}{K_b m^2}}. \tag{16}$$

For circular membrane patches with rotational symmetry about the protein center, the general solution of Eq. (15) is given by [12]

$$u(\rho) = A_u^+ K_0(\sqrt{\nu_+}\rho) + A_u^- K_0(\sqrt{\nu_-}\rho) + B_u^+ I_0(\sqrt{\nu_+}\rho) + B_u^- I_0(\sqrt{\nu_-}\rho), \tag{17}$$

where $I_j(x)$ and $K_j(x)$ are the jth-order modified Bessel functions of the first and second kind, and $A_u^{\pm}$ and $B_u^{\pm}$ are constants to be determined by the boundary conditions at the bilayer-protein interface and at the outer boundary of the membrane patch.

Under the assumption of hydrophobic matching, the value of $u(\rho)$ at the bilayer-protein boundary is fixed by m together with the protein hydrophobic thickness w [Fig. 1(a)]:

$$u(\rho_i) = w - m \equiv U, \tag{18}$$

where U denotes the bilayer-protein hydrophobic mismatch. For reference, we note that for MscS we have $w \approx 1.8$ nm [12,27,28]. Following previous work [41–43] we set here

$$u'(\rho_i) = 0, \tag{19}$$

but note that other choices for $u'(\rho_i)$ are possible [44]. We allow $u(\rho_o)$ to be adjusted freely as part of the minimization procedure, yielding the natural boundary condition [40]

$$\frac{d}{d\rho}\nabla^2 u(\rho) = 0 \tag{20}$$

at $\rho = \rho_o$. Finally, by symmetry we have

$$u'(\rho_o) = 0. \tag{21}$$

With the boundary conditions in Eqs. (18)–(21), the solution of Eq. (15) is given by Eq. (17) with the coefficients

$$A_u^{\pm} = \mp\frac{I_{1o}^{\pm}\Delta Q^{\mp}}{C}U, \quad B_u^{\pm} = \mp\frac{K_{1o}^{\pm}\Delta Q^{\mp}}{C}U, \tag{22}$$

in which $I_{j\eta}^{\pm} = I_j(\sqrt{\nu_{\pm}}\rho_\eta)$, $K_{i\eta}^{\pm} = K_i(\sqrt{\nu_{\pm}}\rho_\eta)$,

$$\Delta Q^{\pm} = Q_{oi}^{\pm} - Q_{io}^{\pm}, \quad Q_{\eta\theta}^{\pm} = \sqrt{\nu_{\pm}} I_{1\eta}^{\pm} K_{1\theta}^{\pm}, \tag{23}$$

and

$$C = \Delta Q^{+}(I_{1o}^{-}K_{0i}^{-} + I_{0i}^{-}K_{1o}^{-}) - \Delta Q^{-}(I_{1o}^{+}K_{0i}^{+} + I_{0i}^{+}K_{1o}^{+}), \tag{24}$$

with $j = 1, 2$, $\eta = i,\ o$, and $\theta = i,\ o$. Substitution of Eq. (17) with Eqs. (22)–(24) into Eq. (14) yields the MPPN thickness deformation energy [12]

$$E_u(n, R) = \frac{n\pi K_b U^2 \rho_i}{C}\Delta Q^{+}\Delta Q^{-}(\nu_{+} - \nu_{-}) \tag{25}$$

for n identical membrane patches.

D. MPPN defect energy

In Secs. II B and II C we assumed a uniform hexagonal arrangement of membrane proteins in MPPNs and, on this basis, obtained [30] the mean-field MPPN midplane and thickness deformation energies in Eqs. (13) and (25), respectively. However, the spherical shape of MPPNs necessitates topological defects in the hexagonal packing of membrane proteins, which incur an n-dependent energy penalty. At the mean-field level, deviations from hexagonal protein packing due to the spherical shape of MPPNs can be quantified [11,12,23], for a given n, through the fraction of the surface of a sphere enclosed by n identical nonoverlapping circles at closest packing [45,46], $p(n)$. Approximating the spring network associated with the energetically preferred hexagonal protein arrangement by a uniform elastic sheet, the leading-order contribution to the MPPN defect energy is thus given by [11,12,23]

$$E_d(n, R) = \frac{K_s}{2}As^2, \tag{26}$$

where K_s is the stretching modulus of the elastic sheet, the MPPN area $A = 4\pi R^2$, and the areal strain $s = [p_{\max} - p(n)]/p_{\max}$ with $p_{\max} = \pi/2\sqrt{3}$ for uniform hexagonal protein arrangements (see Appendix A). The stretching modulus in Eq. (26) is given by [11,12]

$$K_s = \frac{\sqrt{3}}{24n}\frac{\partial^2 E_0}{\partial \rho_o^2}\bigg|_{\rho_o=\rho_o^{\min}}, \tag{27}$$

where $E_0 = E_h + E_u$ [see Eqs. (13) and (25)] and $\rho_o^{\min}$ is the value of ρ_o minimizing E_0 for $\rho_o \geqslant \rho_i$ at a given n. In other words, we estimate the n-dependent energy cost of topological defects in protein packing in MPPNs [Eq. (26) with Eq. (27)] by expanding the MPPN energy about an ideally closed-packed (hexagonal) MPPN state with energy E_0 and $\rho_o = \rho_o^{\min}$. As mentioned in Sec. II A, we take here $10 \leqslant n \leqslant 80$. We use the values of $p(n)$ compiled in Refs. [45,46].

The expression for K_s in Eq. (27) [11,12] can be understood intuitively by dividing the ideally packed, hexagonal protein lattice into triangular area elements with one membrane protein at each corner and taking the membrane proteins to be coupled by Hookean springs with force constant K_0 [11,47]. In our mean-field model of lipid bilayer deformations in MPPNs the (in-plane) membrane protein separation is equal to $2\rho_o$ (see Secs. II B and II C). The side length of each triangular area element is therefore given by $l = 2\rho_o$, with $\rho_o = \rho_o^{\min}$ in the state of the spring network minimizing E_0. If l is deformed by Δl, then the leading-order change in the elastic energy per area element is given by

$$\Delta E_{\text{element}} = \frac{3K_0}{4}(\Delta l)^2, \tag{28}$$

where we have noted that each one of the three springs in each area element contributes equally to the energy of two area elements. Since each area element is associated with one-sixth of three hexagonal unit cells, we also have $E_{\text{element}} = E_0/2n$. From Eq. (28) we thus find

$$K_0 = \frac{1}{12n}\frac{\partial^2 E_0}{\partial \rho_o^2}\bigg|_{\rho_o=\rho_o^{\min}}, \tag{29}$$

from which Eq. (27) follows in the continuum limit via $K_s = \sqrt{3}K_0/2$ [11,47]. As shown in Appendix A, the MPPN defect energy in Eq. (26) can be obtained following similar physical reasoning [11,23,47].

E. Steric constraints

As discussed in Secs. II A–II D, the MPPN energy $E_{\min}(n)$ in Eq. (6) is obtained, at each n, by minimizing $E(n, R)$ in Eq. (7) with respect to R. The value of R and, hence, ρ_o must thereby be large enough to satisfy steric constraints arising from the finite size of lipids and proteins. We assume that these steric constraints result in hardcore steric repulsion between membrane proteins in MPPNs. We denote the smallest value of ρ_o allowed by steric constraints by ρ_o^s [see Fig. 1(b)]. To determine the relation between ρ_o^s and the smallest value

of R allowed by steric constraints, R^s, we need to take into account topological defects in protein packing [11]. In particular, within the mean-field approach used here, the MPPN area occupied by the n nonoverlapping circles associated with the n proteins on the MPPN surface must be equal to $4\pi R^2 p(n)$ [45,46] for spherical MPPN shapes. We thus have

$$\cos\bar{\beta} = 1 - 2\frac{p(n)}{n}, \tag{30}$$

where $\bar{\beta} < \beta$ is the angle subtended by each one of these n circles with respect to the MPPN center, yielding a solid angle $2\pi(1-\cos\bar{\beta})$. Steric constraints mandate $R \geqslant R^s = \rho_o^s/\sin\bar{\beta}$ [Fig. 1(b)]. Equation (30) then implies [11,12]

$$\rho_o^s = 2R^s\sqrt{\frac{p(n)}{n}\left[1-\frac{p(n)}{n}\right]}, \tag{31}$$

which determines, at each n, ρ_o^s in terms of R^s.

Our focus here is on protein steric constraints due to protein domains outside the membrane, which may arise from a well-defined shape of protein domains outside the membrane, entropic repulsion between membrane proteins with flexible domains outside the membrane, or binding of other molecules to membrane proteins. The resulting geometric constraints on MPPNs affect the MPPN self-assembly diagram via Eq. (31). We take the protein domains restricting protein separation in MPPNs to be located on the outside of MPPNs [Fig. 1(b)]. Scenarios in which protein domains on the inside of MPPNs restrict the protein separation in MPPNs could be treated using the same formalism employed here with $h^s \to -h^s$, and analogous conclusions would apply in this case. For protein steric constraints due to protein domains on the outside of MPPNs, R^s depends on the in-plane protein radius outside the membrane, r^s, and on the effective protein height above the midplane of the protein hydrophobic region, h^s [Fig. 1(b)]. From Fig. 1(b) we have

$$\tan\bar{\beta} = \frac{r^s}{R^s - \epsilon + h^s}, \tag{32}$$

where $\bar{\beta}$ is determined by Eq. (30) [Fig. 1(b)]. Note from Fig. 1 that $\epsilon/R = 1-\sqrt{1-(\rho_i/R)^2}$. Taking the protein radius in the bilayer midplane to be small compared to the MPPN size, we simplify Eq. (32) by letting $\epsilon \to 0$. In addition to geometric constraints due to protein domains outside the membrane, the finite size of lipids implies that $\rho_o^s \geqslant \rho_i + \rho_l$ [11,12], where we use here the lipid radius $\rho_l = 0.45$ nm associated with the diC14:0 lipids employed for MPPNs formed from MscS proteins [6,7,48]. Combining Eq. (32) with $\rho_o^s \geqslant \rho_i + \rho_l$ we thus arrive at

$$R^s = \max\left(r^s\cot\bar{\beta} - h^s,\ \frac{\rho_i+\rho_l}{\sin\bar{\beta}}\right), \tag{33}$$

where, as noted above, we have $R^s = \rho_o^s/\sin\bar{\beta}$.

To calculate MPPN self-assembly diagrams, we minimize $E(n,R)$ in Eq. (7) with respect to R subject to the steric constraints on R in Eq. (33), which determine ρ_o^s via Eq. (31). In particular, we calculate $E_{\min}(n)$ as follows. We first note that the contributions $E_h(n,R)$ and $E_u(n,R)$ to $E(n,R)$ in Eq. (7) can be calculated analytically via Eqs. (13) and (25). We thus construct $E_0(n,R) = E_h(n,R) + E_u(n,R)$, and analytically minimize E_0 with respect to ρ_o at each n. If E_0 has a unique minimum $\rho_o = \rho_o^{\min}$, then we calculate K_s via Eq. (29) at this minimum, from which the defect energy $E_d(n,R)$ is obtained via Eq. (26). For large-enough protein-induced lipid bilayer thickness deformations, E_0 can have two minima as a function of ρ_o [12]. In this case, we divide the ρ_o range into two separate search intervals divided by the local maximum in E_0 separating these two local minima. For each n, we minimize $E(n,R)$ in both search intervals using the respective K_s implied by Eq. (29), and choose the value of ρ_o yielding the smallest $E(n,R)$. The minimization of $E(n,R)$ is performed subject to the steric constraints in Eq. (33) with Eq. (31). At each n, we thus obtain the R yielding the smallest $E(n,R)$, $E_{\min}(n)$. Our search for the smallest $E(n,R)$ is done numerically with a precision of approximately 1×10^{-5} nm in R.

III. MPPN SELF-ASSEMBLY DIAGRAMS UNDER PROTEIN STERIC CONSTRAINTS

In this section we use the mean-field model of MPPN self-assembly described in Sec. II to study the effect of protein steric constraints on MPPN shape. Section III A explores how MPPN self-assembly diagrams are modified by finite values of the in-plane protein radius outside the membrane and the effective protein height above the midplane of the protein hydrophobic region. In Sec. III B we construct MPPN self-assembly diagrams as a function of the in-plane protein radius outside the membrane and provide simple mathematical expressions describing the effect of protein steric constraints on MPPN shape.

A. Modifying MPPN self-assembly diagrams through r^s and h^s

As detailed in Sec. II E, we describe here steric constraints arising from protein domains outside the membrane through the in-plane protein radius outside the membrane, r^s, and the effective protein height above the midplane of the protein hydrophobic region, h^s [Fig. 1(b)]. Figure 2 shows MPPN self-assembly diagrams, plotted as a function of the bilayer-protein contact angle α and the absolute value of the bilayer-protein hydrophobic mismatch $|U|$, for selected values of r^s and h^s. Note that since the bilayer thickness deformation energy in Eq. (14) is invariant under $u \to -u$ and we consider here a fixed value of the unperturbed lipid bilayer thickness m, the MPPN self-assembly diagrams calculated here are symmetric under $U \to -U$.

We plot the MPPN self-assembly diagrams in Fig. 2, as well as all other MPPN self-assembly diagrams in this article, as color maps of the MPPN equilibrium distribution $\phi(n)$ in Eq. (6). In particular, we show the $\phi(n)$ for the dominant MPPN n states, and explicitly indicate the values of n associated with dominant MPPNs in selected regions of the MPPN self-assembly diagrams. For a given (dominant) MPPN n state in our model, the symmetry of the corresponding protein arrangement in MPPNs is that associated with the centers of n identical nonoverlapping circles on a spherical surface at closest packing [45,46]. Dominant MPPN n states found here have the symmetry of the icosahedron ($n = 12$), the snub cube ($n = 24$), the face-capped icosahedron

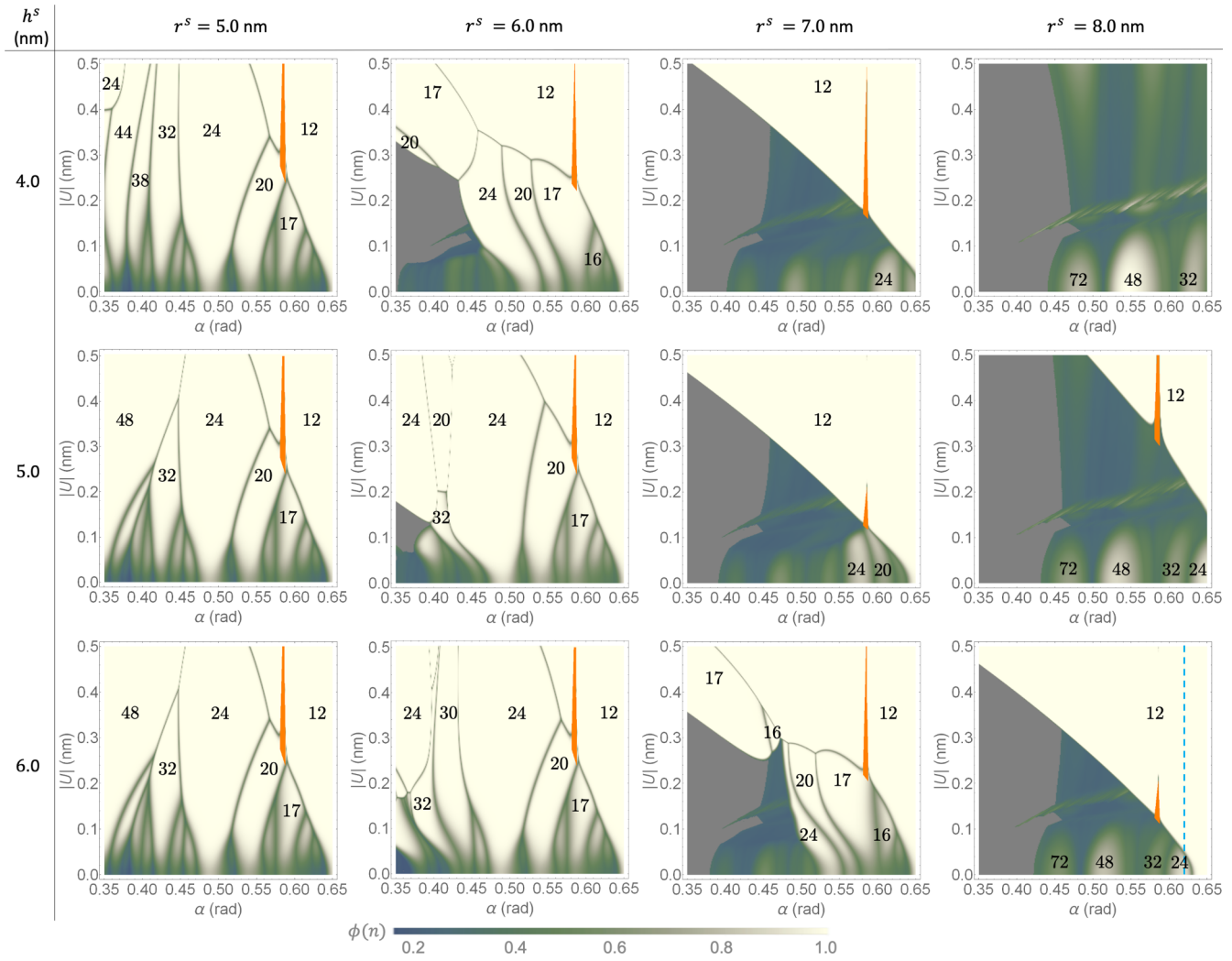

FIG. 2. MPPN self-assembly diagrams as a function of the absolute value of the bilayer-protein hydrophobic mismatch, $|U|$, and the bilayer-protein contact angle, α, for the indicated values of r^s and h^s. The color maps show the maximum values of $\phi(n)$ associated with the dominant MPPN n states, obtained from Eq. (6) for $10 \leqslant n \leqslant 80$. Selected dominant MPPN n states are indicated in the MPPN self-assembly diagrams. Orange shading shows regions of the MPPN self-assembly diagrams for which $n = 12$ is strongly penalized by large values of K_s resulting from $\rho_o^{\min} \to \rho_i$ in Eq. (27) [11,12]. To obtain these regions of the MPPN self-assembly diagrams we recalculated the MPPN self-assembly diagrams with $K_s = 0$ for $n = 12$, and shaded in orange regions of the MPPN self-assembly diagrams for which these modified calculations yield a different dominant MPPN n state. As noted in the main text, the continuum model of MPPN bilayer mechanics used here may not give reliable results in the orange-shaded regions of the MPPN self-assembly diagrams. Gray shading indicates regions of the MPPN self-assembly diagrams, where $n = 80$ gives the dominant MPPN n state, which may be a spurious result of our constraint $10 \leqslant n \leqslant 80$. The dashed vertical line in the bottom-right panel corresponds to $\alpha = 0.62$ rad.

($n = 32$), the snub cuboctahedron ($n = 48$), and a modified snub dodecahedron ($n = 72$) [45,46,49]. In the regions of the MPPN self-assembly diagrams in Fig. 2 for which these MPPN n states are dominant, the corresponding ranges in the MPPN radii are given by 7.0 nm $\lessapprox R \lessapprox$ 7.9 nm ($n = 12$), 9.8 nm $\lessapprox R \lessapprox$ 15 nm ($n = 24$), 11 nm $\lessapprox R \lessapprox$ 20 nm ($n = 32$), 14 nm $\lessapprox R \lessapprox$ 26 nm ($n = 48$), and 21 nm $\lessapprox R \lessapprox$ 32 nm ($n = 72$). We do not distinguish in this article between different chiral states of MPPNs.

As implied by Eq. (33), steric effects on MPPN self-assembly diagrams due to protein domains outside the membrane become increasingly pronounced with increasing r^s and decreasing h^s (Fig. 2). For instance, the MPPN self-assembly diagram in the lower-left panel of Fig. 2 corresponding to $r^s = 5.0$ nm and $h^s = 6.0$ nm is not affected by r^s and h^s, and an identical MPPN self-assembly diagram would be obtained if no steric constraints due to protein domains outside the membrane had been imposed [12]. In particular, the molecular structure of MscS [27,28] yields $r^s \approx 4.0$ nm and $h^s \approx 11.0$ nm, which means that the dominant steric constraints in Eq. (33) with Eq. (31) are set by the MscS radius in the bilayer midplane and the finite size of lipids, rather than MscS domains outside the membrane. The MPPN self-assembly diagrams obtained here for MPPNs formed from MscS thus agree with previous calculations of MPPN self-assembly diagrams for MPPNs formed from MscS [11,12], which successfully predict the observed symmetry and size of MPPNs formed from MscS [6,7]. As noted in Sec. II B

we use here the lipid bilayer bending rigidity $K_b = 14\ k_BT$ measured for the diC14:0 lipids used for MPPNs formed from MscS [6,7,39]. While the broad features of the MPPN self-assembly diagrams obtained here do not depend on the precise value of K_b used [12,39], we note that changes in K_b can shift the boundaries separating regions of the MPPN self-assembly diagrams dominated by distinct MPPN n states (see Appendix B).

As pointed out before [11,12], in the limit $\rho_o^{\min} \to \rho_i$ Eq. (27) can yield large K_s and, hence, suppress dominant MPPN n states. In practice, steric constraints on lipid size are expected to prohibit $\rho_o^{\min} \to \rho_i$, and the continuum model of MPPN bilayer mechanics used here may not give reliable results in this limit. In the MPPN self-assembly diagrams considered here this issue only arises for MPPNs with $n = 12$. We highlight the corresponding regions in MPPN self-assembly diagrams by orange shading. We also highlight, through gray shading, regions in MPPN self-assembly diagrams for which $n = 80$ gives the dominant MPPN n state. The dominance of MPPNs with $n = 80$ in these regions of parameter space may be a spurious result arising from the constraint $10 \leqslant n \leqslant 80$ in the calculations described here.

As r^s is increased at fixed h^s, protein steric constraints increasingly perturb the MPPN self-assembly diagrams, and lead to shifts in the boundaries separating regions of the MPPN self-assembly diagrams dominated by distinct MPPN n states (Fig. 2). Intriguingly, protein steric constraints are seen to have two competing effects on the predicted MPPN symmetries. On the one hand, protein steric constraints can effectively rule out dominant MPPN n states, leaving large portions of the MPPN self-assembly diagrams with no clearly defined MPPN symmetry. On the other hand, suitable combinations of r^s and h^s can greatly expand the portions of the MPPN self-assembly diagrams dominated by highly symmetric MPPN n states. In particular, for the scenarios considered in Fig. 2 protein steric constraints can strongly increase the dominance of MPPN states with icosahedral symmetry ($n = 12$).

We note from Fig. 2 that protein steric constraints manifest themselves differently for different MPPN n states. In particular, regions in the MPPN self-assembly diagrams in Fig. 2 dominated by larger, less symmetric MPPN n states tend to be affected more strongly by protein steric constraints than regions dominated by smaller, more symmetric MPPN n states. As discussed in greater detail in Sec. III B, this can be understood from the mathematical representation of protein steric constraints in Sec. II E. In particular, from Eq. (33) we see that steric constraints arising from protein domains outside the membrane yield the constraint $R \geqslant r^s \cot\bar{\beta} - h^s$. From Eq. (30) we have $\bar{\beta} = \arccos[1 - 2p(n)/n]$. Thus, MPPN n states with larger n and smaller $p(n)$ are governed by a more stringent lower bound on R and, hence, are affected more strongly by protein steric constraints. As a result, protein steric constraints can bias MPPN self-assembly toward smaller, more symmetric MPPN states at the expense of larger, less symmetric MPPN states (see Fig. 2).

To gain further insight into the competition between different MPPN n states in Fig. 2 it is useful to examine the dominant MPPN n states along the vertical dashed line $\alpha = 0.62$ rad in the lower-right panel of Fig. 2. Accord-

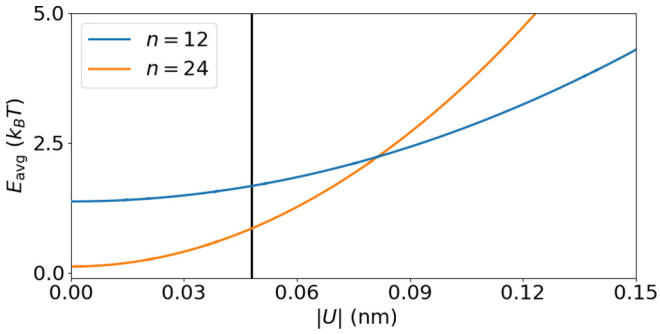

FIG. 3. MPPN energy per protein, $E_{avg}(n) = E_{min}(n)/n$, as a function of the absolute value of the bilayer-protein hydrophobic mismatch, $|U|$, for $\alpha = 0.62$ rad, $r^s = 8.0$ nm, and $h^s = 6.0$ nm. The MPPN states $n = 12$ and $n = 24$ considered here are the dominant MPPN n states along the dashed vertical line in the MPPN self-assembly diagram in the bottom-right panel of Fig. 2. The vertical solid line corresponds to $|U| = 0.048$ nm, for which the dominant MPPN n state transitions from $n = 24$ to $n = 12$ in the MPPN self-assembly diagram in the bottom-right panel of Fig. 2.

ing to the MPPN self-assembly diagram in Fig. 2, the two dominant MPPN n states along this line are $n = 12$ and $n = 24$, respectively. Figure 3 shows the corresponding average MPPN energies per protein, $E_{avg}(n) = E_{min}(n)/n$, as a function of $|U|$. We note from Fig. 3 that, as one increases $|U|$, MPPNs with $n = 12$ can become dominant even though $E_{avg}(12) > E_{avg}(24)$. This can be understood by noting that the Boltzmann weight for each MPPN n state is given by $\exp\{n[\mu - E_{avg}]/k_BT\}$ [see Eq. (4)]. In the dilute limit $c \ll 1$, Eq. (5) implies $\mu - E_{avg}(n) < 0$. As a result, thermal effects penalize MPPN n states with larger n, and can make an MPPN n state with decreased n (such as $n = 12$) dominant even if this MPPN n state does not correspond to the state with minimal E_{avg}. Thus, thermal effects can combine with protein steric constraints to bias MPPN self-assembly toward smaller, more symmetric MPPN states.

B. Quantifying the effect of protein steric constraints on MPPN self-assembly diagrams

Figure 4 shows MPPN self-assembly diagrams, plotted as a function of the bilayer-protein contact angle α and the in-plane protein radius outside the membrane r^s, for $h^s = 3.0$ nm and $h^s = 5.0$ nm with $U = 0$ (see also Appendix C). Note from Fig. 4 that, in the small-r^s regime, the dominant MPPN symmetry is independent of r^s. Conversely, Fig. 4 shows that, for large-enough r^s, the dominant MPPN symmetry has a strong dependence on r^s. We find that, for large-enough r^s, steric constraints due to protein domains outside the membrane can substantially expand the regions of MPPN self-assembly diagrams dominated by highly symmetric MPPN n states, such as MPPNs with $n = 48$ and $n = 72$ in Fig. 4. In Fig. 4(b), the ranges of MPPN radii associated with dominant MPPN n states in the MPPN self-assembly diagram are given by 7.0 nm $\lessapprox R \lessapprox$ 8.2 nm ($n = 12$), 9.8 nm $\lessapprox R \lessapprox$ 17 nm ($n = 24$), 11 nm $\lessapprox R \lessapprox$ 20 nm ($n = 32$), 16 nm $\lessapprox R \lessapprox$ 26 nm ($n = 48$), and 25 nm $\lessapprox R \lessapprox$ 34 nm ($n = 72$). In Fig. 4(c), which shows the same data as Fig. 4(a) but with an

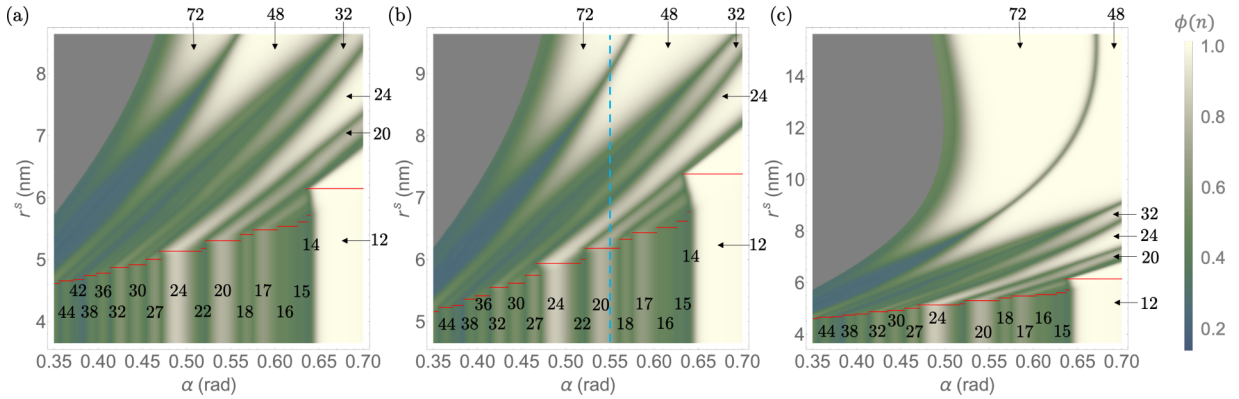

FIG. 4. MPPN self-assembly diagrams as in Fig. 2 but as a function of the bilayer-protein contact angle, α, and the in-plane protein radius outside the membrane, r^s, at $U = 0$ with (a) $h^s = 3.0$ nm, (b) $h^s = 5.0$ nm, and (c) $h^s = 3.0$ nm for an extended r^s range, respectively. We use the same notation as in Fig. 2. The r^s coordinates of the horizontal red lines are given by $r_0^s(n)$ in Eq. (34). Each red line is drawn from the left to the right α-boundary of the MPPN region dominated by a given MPPN n state. We use the same color scheme for all three panels. The blue dashed vertical line in panel (b) corresponds to $\alpha = 0.55$ rad.

extended r^s range, the corresponding ranges of MPPN radii are given by 7.0 nm $\lessapprox R \lessapprox$ 8.1 nm ($n = 12$), 9.8 nm $\lessapprox R \lessapprox$ 18 nm ($n = 24$), 11 nm $\lessapprox R \lessapprox$ 24 nm ($n = 32$), 14 nm $\lessapprox R \lessapprox$ 54 nm ($n = 48$), and 21 nm $\lessapprox R \lessapprox$ 68 nm ($n = 72$).

Following Sec. III A it is instructive to consider the smallest r^s for which protein domains outside the membrane can affect MPPN self-assembly diagrams, r_0^s. From Eq. (33) we find

$$r_0^s(n) = \frac{\rho_i + \rho_l}{\cos\bar{\beta}} + h^s \tan\bar{\beta}. \tag{34}$$

At small r^s, the MPPN self-assembly diagrams in Fig. 4 are divided into bands along the α axis within which distinct MPPN n states are dominant. We indicate in Fig. 4 the corresponding r_0^s obtained from Eq. (34) (horizontal lines in Fig. 4). In general, Eq. (34) provides good estimates of the smallest values of r^s in Fig. 4 for which steric constraints due to protein domains outside the membrane start to affect MPPN self-assembly diagrams. However, some notable discrepancies are obtained for highly symmetric MPPN n states, such as $n = 12$, 20, and 24 in Fig. 4. With increasing r^s, the regions of the MPPN self-assembly diagrams in Fig. 4 dominated by such highly symmetric MPPN n states are seen to "expand," even at $r^s < r_0^s$, into neighboring regions of the MPPN self-assembly diagrams dominated, as $r^s \to 0$, by less symmetric MPPN n states. This can be understood from Fig. 5, which shows $r_0^s(n)$ in Eq. (34) for $10 \leqslant n \leqslant 30$. We find that, while r_0^s generally tends to decrease with increasing n, $r_0^s(n)$ exhibits local maxima at $n = 12$, 20, and 24. Equation (30) implies that $\bar{\beta}$ monotonically increases with $p(n)$ for $10 \leqslant n \leqslant 80$, with $p(n)$ showing local maxima at $n = 12$, 20, and 24 [45,46]. As a result, one finds from Eq. (34) that, for such highly symmetric MPPN n states, larger r^s are required to affect the minimum MPPN energy $E_{\min}(n)$. Regions in the MPPN self-assembly diagrams dominated by highly symmetric MPPN n states are thus effectively less constrained by r^s than neighboring regions in the MPPN self-assembly diagrams dominated by less symmetric MPPN n states, allowing expansion of regions of MPPN self-assembly diagrams dominated by highly symmetric MPPN n states with increasing r^s.

To understand some of the key features of Fig. 4 in the regime $r^s > r_0^s$, we note that protein steric constraints only provide lower bounds on R. As explained in Sec. II, the value of R and, hence, ρ_o is determined at each n through minimization of $E(n, R)$ in Eq. (7) with respect to R. Assuming $\alpha > \beta$ and neglecting, for simplicity, all contributions to E apart from E_h, MPPNs attain their minimum-energy state at the membrane patch radius

$$\rho_o = \frac{a}{b}\rho_i \tag{35}$$

with $E_h = 0$, which follows directly from Eq. (13). We define r_h^s as the value of r^s for which the smallest value of ρ_o allowed by protein steric constraints is equal to ρ_o in Eq. (35). For $r^s > r_h^s$, protein steric constraints thus prohibit MPPNs from attaining the value of ρ_o in Eq. (35). From Eq. (33) with Eq. (35) we find

$$r_h^s(n) = \frac{a}{b\cos\bar{\beta}}\rho_i + h^s \tan\bar{\beta}. \tag{36}$$

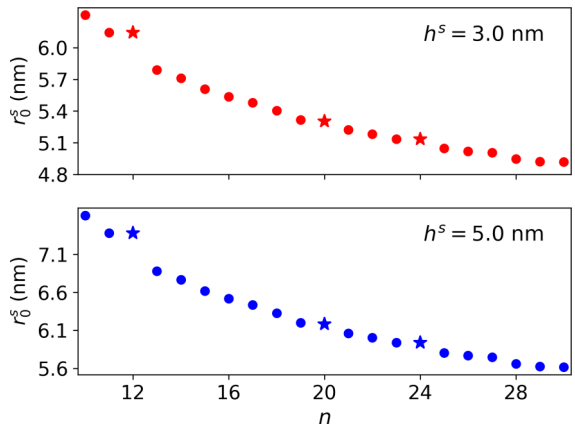

FIG. 5. Estimates of the smallest r^s for which protein domains outside the membrane can affect MPPN self-assembly diagrams, r_0^s, in Eq. (34) versus n at $h^s = 3.0$ nm (upper panel) and $h^s = 5.0$ nm (lower panel). The highly symmetric MPPN n states with $n = 12$, 20, and 24 are marked with star symbols.

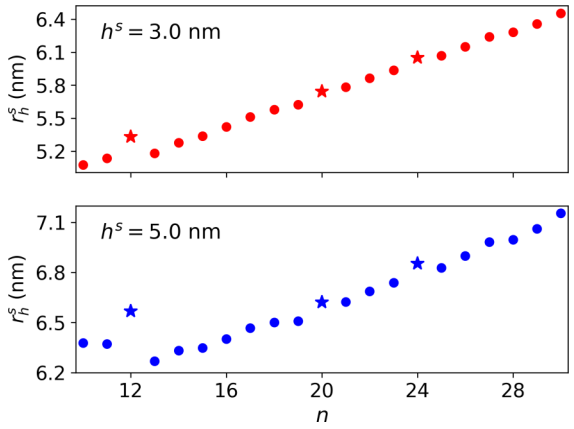

FIG. 6. Smallest r^s estimated to affect the MPPN patch size at $U = 0$ in Eq. (36), r_h^s, versus n at $h^s = 3.0$ nm (upper panel) and $h^s = 5.0$ nm (lower panel). As in Fig. 5, the highly symmetric MPPN n states with $n = 12$, 20, and 24 are marked with star symbols.

Note that Eq. (35) does not include any contributions due to the defect energy E_d. Even for $U = 0$, the simple estimate of r_h^s in Eq. (36) therefore only holds approximately (see also Appendix C).

Figure 6 shows $r_h^s(n)$ in Eq. (36) for $10 \leqslant n \leqslant 30$. In contrast to $r_0^s(n)$ in Eq. (34) (Fig. 5), we find that r_h^s generally tends to increase with increasing n. Thus, larger n require a larger value of r^s to affect the estimate of ρ_o in Eq. (35). This suggests that, in the regime $r^s > r_0^s$, protein steric constraints bias MPPN self-assembly toward MPPN n states with larger n, which is indeed borne out by the results in Fig. 4. Note that, since we assumed $E_u = 0$ in Eq. (36), Eq. (36) is not expected to apply to the large-$|U|$ regime in Fig. 2. Similarly as r_0^s in Fig. 5, r_h^s in Fig. 6 exhibits local maxima at highly symmetric MPPN n states. As for Eq. (34), this can be understood based on Eq. (36) by noting from Eq. (30) that $\bar{\beta}$ monotonically increases with $p(n)$ for $10 \leqslant n \leqslant 80$, with $p(n)$ showing local maxima at $n = 12$, 20, and 24 [45,46]. Thus, not only for $r^s < r_0^s$ but also for $r^s > r_0^s$ highly symmetric MPPN n states are less stringently restricted by protein steric constraints than less symmetric MPPN n states with similar n, effectively biasing MPPN self-assembly toward highly symmetric MPPN n states for $r^s > r_0^s$ as well as for $r^s < r_0^s$ in Fig. 4.

Figure 7 shows the MPPN radius R (upper panel) and the MPPN energy per protein $E_{\rm avg}$ (lower panel) as a function of r^s along the line $\alpha = 0.55$ rad in Fig. 4(b) for selected, dominant MPPN n states. We find that, consistent with r_h^s in Eq. (36), smaller MPPN n states start to increase in size at smaller r^s. However, Fig. 7 also shows that transitions between different dominant MPPN n states do not coincide exactly with the onset of r^s-induced increases in MPPN size. This illustrates that, as anticipated above, Eq. (36) only provides an approximate measure of transitions between dominant MPPN n states. The lower panel of Fig. 7 shows that, as r^s is increased, MPPNs with smaller n can be dominant even if they have a larger energy per protein than competing MPPN n states with larger n. As in Fig. 3, this effect results from entropic contributions to the free energy of the system.

Finally, we consider the effect of a finite U on the MPPN self-assembly diagrams in Fig. 4. In particular, we set

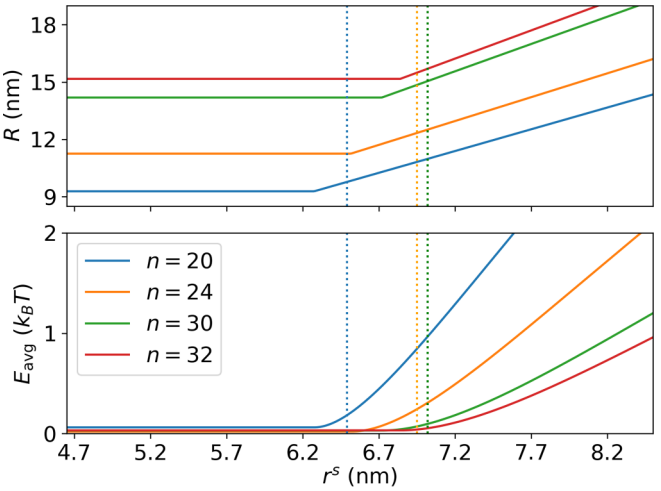

FIG. 7. MPPN radii R (upper panel) and corresponding MPPN energy per protein $E_{\rm avg}(n) = E_{\rm min}(n)/n$ (lower panel) versus in-plane protein radius outside the membrane, r^s. As in Fig. 4(b), we set $h^s = 5.0$ nm and $U = 0$. We use here $\alpha = 0.55$ rad, which corresponds to the dashed vertical line in Fig. 4(b), and consider the first four dominant MPPN n states (starting from small r^s) along this line in Fig. 4(b). The dashed vertical lines indicate transitions from $n = 20$ to $n = 24$, from $n = 24$ to $n = 30$, and from $n = 30$ to $n = 32$ (left to right) in the dominant MPPN n state in the MPPN self-assembly diagram in Fig. 4(b).

$|U| = 0.2$ nm with, as in Fig. 4(b), $h^s = 5.0$ nm (see Fig. 8). Comparing Fig. 4(b) and Fig. 8 we find that, in the small r^s-regime, a finite U can strongly bias MPPN self-assembly toward highly symmetric MPPN n states [12]. Furthermore, Fig. 8 shows that large r^s can prevent the dominance of highly symmetric MPPN n states at finite $|U|$. This is in marked contrast to the results obtained in Fig. 4 at $U = 0$. But we also note from Fig. 2 that, for large-enough α, the interplay of

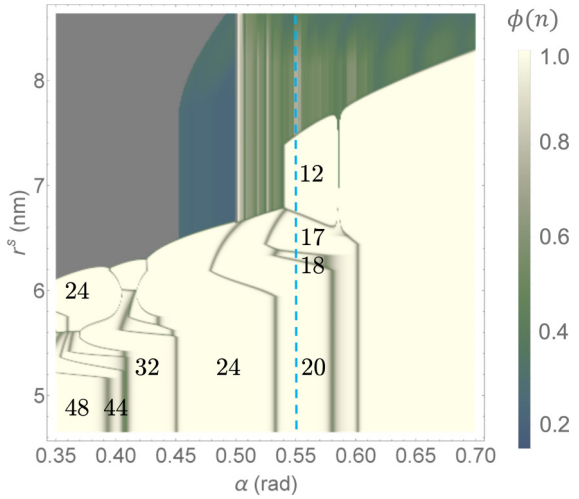

FIG. 8. MPPN self-assembly diagram as in Fig. 4(b) for $h^s = 5.0$ nm but with $|U| = 0.2$ nm. The blue dashed vertical line corresponds to $\alpha = 0.55$ rad, for which the dominant MPPN n states are $n = 20$, 18, 17, and 12 (from bottom to top). We use the same notation as in Fig. 2.

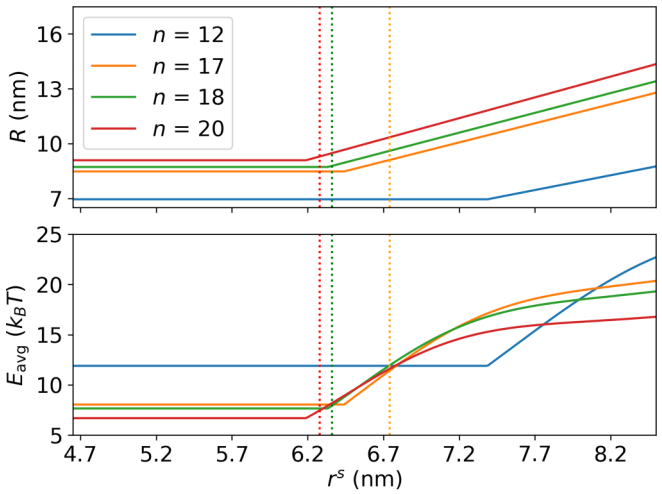

FIG. 9. MPPN radii R (upper panel) and corresponding MPPN energy per protein $E_{avg} = E(n)/n$ (lower panel) versus in-plane protein radius outside the membrane, r^s. As in Fig. 8, we set $h^s = 5.0$ nm and $|U| = 0.2$ nm. We use here $\alpha = 0.55$ rad, which corresponds to the dashed vertical line in Fig. 8, and consider the first four dominant MPPN n states (starting from small r^s) along this line in Fig. 8. The dashed vertical lines indicate transitions from $n = 20$ to $n = 18$, from $n = 18$ to $n = 17$, and from $n = 17$ to $n = 12$ (left to right) in the dominant MPPN n state in the MPPN self-assembly diagram in Fig. 8.

large r^s and large $|U|$ can strongly amplify the dominance of highly symmetric MPPN n states, such as $n = 12$. The ranges of MPPN radii associated with dominant MPPN n states in the MPPN self-assembly diagram in Fig. 8 are given by 7.0 nm $\lessapprox R \lessapprox$ 8.4 nm ($n = 12$), 9.8 nm $\lessapprox R \lessapprox$ 12 nm ($n = 24$), 11 nm $\lessapprox R \lessapprox$ 13 nm ($n = 32$), and 14 nm $\lessapprox R \lessapprox$ 15 nm ($n = 48$).

Similarly as in Fig. 7, we plot in Fig. 9 the MPPN radius R (upper panel) and the MPPN energy per protein E_{avg} (lower panel) as a function of r^s along the line $\alpha = 0.55$ rad in Fig. 8 for selected, dominant MPPN n states. The upper panel in Fig. 9 shows that, contrary to the results obtained at $U = 0$ in Fig. 7, MPPN n states with smaller n start to expand in size at larger r^s than MPPN n states with larger n along the line $\alpha = 0.55$ rad in Fig. 8. As expected from Fig. 7 the lower panel of Fig. 9 shows that, as one increases r^s, MPPNs with larger n can cease to be dominant even if they have a smaller energy per protein than competing MPPN n states with smaller n. Again, this effect results from entropic contributions to the free energy of the system.

IV. SUMMARY AND CONCLUSIONS

We have explored here the effect of protein steric constraints on the symmetry of MPPNs [6,7]. Steric constraints on the separation of membrane proteins in MPPNs arise, on the one hand, within the membrane due to the finite size of proteins and lipids [11,12]. On the other hand, protein domains outside the membrane can produce steric constraints on the separation of membrane proteins in MPPNs. Such protein steric constraints may originate from a well-defined shape of protein domains outside the membrane, entropic repulsion between membrane proteins with flexible domains outside the membrane, or binding of other molecules to membrane proteins. We describe here protein steric constraints in MPPNs based on the in-plane protein radius outside the membrane, r^s, and the effective protein height above the midplane of the protein hydrophobic region, h^s [Fig. 1(a)]. We assume that protein steric constraints induce hardcore steric repulsion between membrane proteins in MPPNs. A more detailed molecular model of protein steric constraints in MPPNs would, for instance, allow for a competition between attractive and repulsive protein interactions outside the membrane.

Our calculations of the effect of protein steric constraints on MPPN symmetry are based on an extension of the mean-field approach developed in Refs. [11,12]. The mean-field approach in Refs. [11,12] successfully predicts, with all model parameters determined directly by experiments, the observed symmetry and size of MPPNs formed from MscS proteins [6,7]. Our calculations show that, for the molecular structure of MscS [27,28], steric constraints due to protein regions outside the membrane do not affect MPPN self-assembly diagrams. Our results on MPPNs formed from MscS [6,7] therefore agree with those in Refs. [11,12] and experiments on MPPNs formed from MscS [27,28]. Our model of MPPN self-assembly could be developed further in a number of different ways. In particular, our mean-field model allows for thermal effects during MPPN self-assembly [11,12,21–23] but assumes that, for each MPPN n state, the dominant MPPN shape corresponds to that with the lowest (elastic) energy. Thermal fluctuations are expected to perturb the MPPN shape about the lowest-energy state. Furthermore, we note that topological defects in protein packing in MPPNs are captured in our mean-field model via the packing fraction $p(n)$ [23,45,46], which has two key limitations. On the one hand, our mean-field approach assumes a uniform protein composition. While justified for the scenarios considered here, this assumption is violated if, for instance, MPPNs are composed of proteins with heterogeneous size. We have previously used a minimal molecular model of MPPN symmetry [20] to explore the shape of MPPNs in this latter scenario. On the other hand, to make our calculations more tractable we assumed in our mean-field approach a circular unit cell. In principle, our approach could be extended to consider, for instance, the polygonal unit cells suggested by the polyhedral symmetry of MPPNs. In analogy to recent work on the physics of protein shells [50,51], such an extension of our approach would allow investigation of the interaction of protein packing defects in MPPNs.

We find that protein steric constraints can strongly affect MPPN self-assembly. On the one hand, our calculations show that protein steric constraints can effectively rule out dominant MPPN states, leaving large portions of the MPPN self-assembly diagrams with no clearly defined MPPN symmetry. On the other hand, we also find that suitable values of r^s and h^s can substantially expand the regions of MPPN self-assembly diagrams dominated by highly symmetric MPPN states, such as MPPNs with icosahedral or snub cube symmetry. For small-enough r^s or large-enough h^s, MPPN self-assembly is independent of protein steric constraints. For scenarios with negligible bilayer-protein hydrophobic mismatch we find that, as r^s is increased or h^s decreased, protein steric constraints

tend to imply more stringent constraints on membrane protein separation in MPPNs for larger, less symmetric MPPN states, thus biasing MPPN self-assembly toward smaller, more symmetric MPPN states. Our calculations suggest that, on further increasing r^s or decreasing h^s, the dominant MPPN states can be shifted toward larger, highly symmetric MPPNs. Finally, we find that a substantial bilayer-protein hydrophobic mismatch biases MPPN self-assembly toward highly symmetric MPPN states for weak protein steric constraints [12] and can, depending on the bilayer-protein contact angle, prevent or amplify the dominance of highly symmetric MPPN states for strong protein steric constraints.

MPPNs have been proposed [6] as a strategy for the structural analysis of membrane proteins under physiologically relevant transmembrane gradients, and as a method for targeted drug delivery with precisely controlled release mechanisms through, for instance, the gating of ion channels in MPPNs. Such applications of MPPNs require control over the number of proteins in MPPNs, and the MPPN symmetry and size. One avenue for controlling MPPN protein composition and shape is to tune the bilayer-protein hydrophobic mismatch in MPPNs [12] through changes in lipid composition [39,52] or repositioning of amphipathic protein residues [53]. The work described here suggests that protein steric constraints provide a complementary approach for the control of MPPN protein composition and shape. For instance, our results imply that targeted binding of proteins of specified size, or of nanoparticles such as quantum dots [54], to membrane proteins could be used to bias MPPN self-assembly toward highly symmetric MPPN states with, depending on the protein or nanoparticle size, small or large MPPN sizes and protein numbers. Modification of protein steric constraints may thus allow the directed self-assembly of MPPNs with specified symmetry, size, and protein composition, facilitating the utilization of MPPNs for high-resolution structural studies of membrane proteins or targeted drug delivery.

ACKNOWLEDGMENTS

We thank O. Kahraman, D. Li, and M. H. B. Stowell for helpful discussions. This work was supported by NSF Award No. DMR-1554716 and the USC Center for High-Performance Computing.

APPENDIX A: PHYSICAL MODEL OF THE MPPN DEFECT ENERGY

Following Ref. [11], we develop here a physical model of the MPPN defect energy $E_d(n, R)$ in Eq. (26). We first note that, in the continuum limit, the elastic (compression or expansion) energy of a hexagonal network of harmonic springs is given by [47]

$$\mathscr{H} = \frac{K}{2}\int dx_1 dx_2 (\nabla \boldsymbol{r})^2, \tag{A1}$$

where K is the continuum force constant and $(\nabla \boldsymbol{r})^2 = (\partial \boldsymbol{r}/\partial x_1)^2 + (\partial \boldsymbol{r}/\partial x_2)^2$, in which x_1 and x_2 are internal coordinates and $\boldsymbol{r} = \boldsymbol{r}(x_1, x_2)$ denotes the external coordinate specifying the location of the surface in the (three-dimensional) embedding space. We relate the elastic energy of the spring network to its areal strain by considering a flat, rectangular patch of a uniform, elastic sheet. We denote the width and height of the rectangular patch by L_1 and L_2, respectively. If L_1 and L_2 are slightly compressed or expanded by ΔL_1 and ΔL_2, respectively, then a point in the patch originally at $\boldsymbol{r}_0(x_1, x_2)$ is translated to

$$\boldsymbol{r}(x_1, x_2) = \boldsymbol{r_0} + \frac{\Delta L_1}{L_1} x_1 \boldsymbol{i} + \frac{\Delta L_2}{L_2} x_2 \boldsymbol{j}, \tag{A2}$$

where $\boldsymbol{i}$ and $\boldsymbol{j}$ are orthogonal unit vectors. We thus have

$$(\nabla \boldsymbol{r})^2 = \left(\frac{\Delta L_1}{L_1}\right)^2 + \left(\frac{\Delta L_2}{L_2}\right)^2. \tag{A3}$$

Furthermore, since the original (unperturbed) area of the rectangular patch is given by $A = L_1 L_2$, the perturbations ΔL_1 and ΔL_2 change, to leading order, the area of the rectangular patch by

$$\Delta A = L_1 \Delta L_2 + L_2 \Delta L_1. \tag{A4}$$

For uniform strain we have $\Delta L_1/L_1 = \Delta L_2/L_2$, in which case Eqs. (A3) and (A4) yield

$$\left(\frac{\Delta A}{A}\right)^2 = 2(\nabla \boldsymbol{r})^2. \tag{A5}$$

The continuum force constant K in Eq. (A1) is related to the discrete force constant of the Hookean springs, K_0 in Eq. (29), via $K = \sqrt{3}K_0$ [47]. Thus, Eq. (A5) implies that Eq. (A1) can be rewritten as

$$\mathscr{H} = \frac{\sqrt{3}K_0}{4}\int dx_1 dx_2 \left(\frac{\Delta A}{A}\right)^2. \tag{A6}$$

For uniform areal strain $\Delta A/A$ is constant and, to leading order, Eq. (A6) can be simplified [1] to

$$\mathscr{H} = \frac{K_s}{2} A \left(\frac{\Delta A}{A}\right)^2 \tag{A7}$$

with, as in Sec. II D, the stretching modulus

$$K_s = \frac{\sqrt{3}K_0}{2} \tag{A8}$$

of the elastic sheet. Similarly as in previous work on viral capsid self-assembly [23] we approximate, at the mean-field level, the areal strain due to topological defects in protein packing in MPPNs by

$$\frac{\Delta A}{A} = \frac{p_{\max} - p(n)}{p_{\max}}. \tag{A9}$$

In Eq. (A9) it is assumed that the average energy penalty due to topological defects in protein packing in MPPNs can be captured, for each MPPN n state, by a uniform areal strain corresponding to the percentage difference between the optimal protein packing fraction allowed by topological constraints and the packing fraction associated with the hexagonal protein arrangement, $p_{\max}$, favored in the absence of topological constraints [23,45,46]. Substitution of Eq. (A9) into the expression for $\mathscr{H}$ in Eq. (A7) results in the MPPN defect energy E_d in Eq. (26).

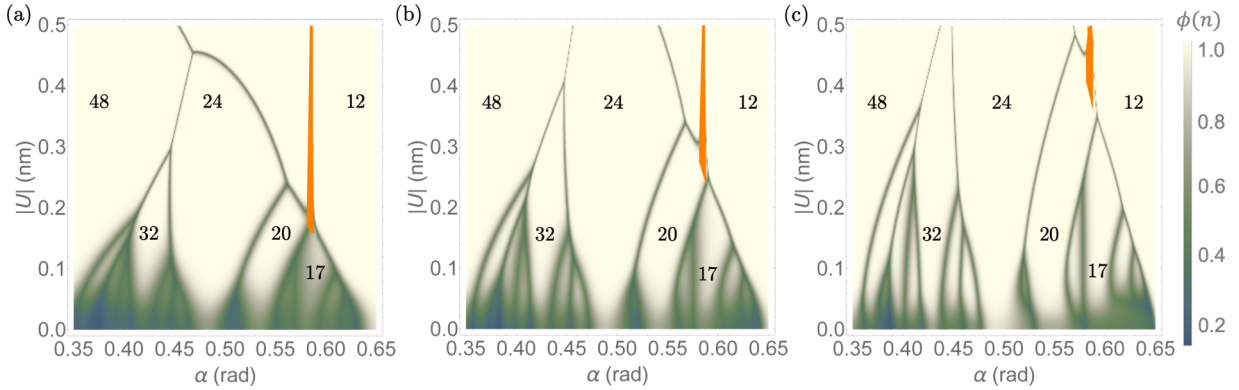

FIG. 10. MPPN self-assembly diagrams as a function of the absolute value of the bilayer-protein hydrophobic mismatch, $|U|$, and the bilayer-protein contact angle, α, for $r^s = 5.0$ nm and $h^s = 6.0$ nm calculated as in Fig. 2 with (a) $K_b = 7\ k_BT$, (b) $K_b = 14\ k_BT$, and (c) $K_b = 28\ k_BT$. The MPPN self-assembly diagram in panel (b) is identical to that in the lower-left panel of Fig. 2 and reproduced here for ease of comparison. We use the same notation as in Fig. 2.

APPENDIX B: EFFECT OF CHANGES IN THE LIPID BILAYER BENDING RIGIDITY ON MPPN SELF-ASSEMBLY DIAGRAMS

Our focus in this article is on lipid bilayers with elastic properties corresponding to the diC14:0 lipids used for MPPNs formed from MscS proteins [6,7,39]. In particular, we use the lipid bilayer bending rigidity $K_b = 14\ k_BT$ [39]. To explore to what extent our results are sensitive to changes in K_b, we consider in Fig. 10 MPPN self-assembly diagrams for the same scenario as in the lower-left panel of Fig. 2 ($r^s = 5.0$ nm and $h^s = 6.0$ nm) with $K_b = 7\ k_BT$ [see Fig. 10(a)], $K_b = 14\ k_BT$ [see Fig. 10(b)], and $K_b = 28\ k_BT$ [see Fig. 10(c)]. The results in Fig. 10(b) are identical to those in the lower-left panel of Fig. 2, and are reproduced here for ease of comparison. The range in K_b considered in Fig. 10 approximately corresponds to the range in K_b measured for phospholipid bilayers with distinct lipid tail lengths [5,39]. We find in Fig. 10 that the broad features of the MPPN self-assembly diagrams obtained here do not depend on the precise value of K_b used [12]. However, we also find that changes in K_b can shift the boundaries separating regions of the MPPN self-assembly diagrams dominated by distinct MPPN n states. In particular, as K_b is increased in Fig. 10, larger $|U|$ are required to produce transitions in MPPN symmetry from large-n (lower symmetry) MPPN states to small-n (higher symmetry) MPPN states. Thus, the MPPN self-assembly diagrams in Fig. 10 are, from left to right, effectively "stretched out" in the direction of increasing $|U|$.

APPENDIX C: VANISHING PROTEIN HEIGHT

In this Appendix we consider the limiting case of a vanishing protein height, $h^s \to 0$, in our model of MPPN self-assembly (Fig. 1). While this limiting case has no direct physical significance, it provides insight into the mathematical properties of the mean-field model of MPPN self-assembly considered here. We focus on the small-r^s regime, where protein steric constraints due to r^s only produce small perturbations of MPPN self-assembly diagrams. For simplicity, we also set $U = 0$ throughout this Appendix. For $h^s = 0$, Eq. (36) simplifies to

$$r_h^s(n) = \frac{a}{b\cos\bar{\beta}}\rho_i. \tag{C1}$$

The boundaries delineating regions in the α-r^s plane of MPPN self-assembly diagrams dominated by distinct MPPN n states can thus be estimated from

$$\mathscr{B}(\alpha, n) = r_h^s + \mathscr{C}, \tag{C2}$$

where $\mathscr{C}$ depends on n but is constant with α. Figure 11 shows Eq. (C2) together with the corresponding MPPN self-assembly diagram at $h^s = 0$. We thereby fix $\mathscr{C}$ so that, at each n, $\mathscr{B}(\alpha, n)$ in Eq. (C2) coincides with $r_0^s(n)$ in Eq. (34) at the small-α boundary of the MPPN region dominated

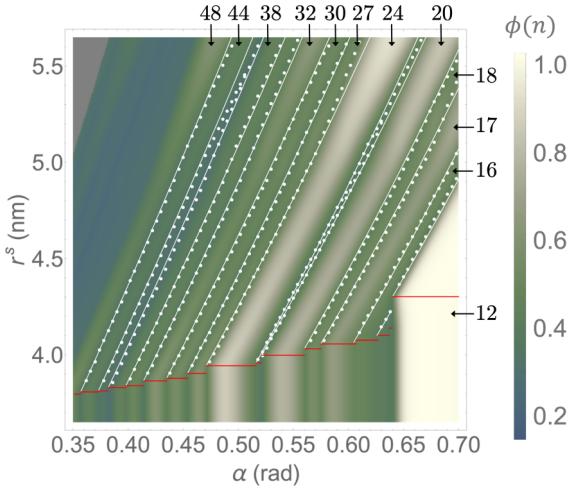

FIG. 11. MPPN self-assembly diagram as in Fig. 4 as a function of the bilayer-protein contact angle, α, and the in-plane protein radius outside the membrane, r^s, at $U = 0$ in the (nonphysical) case $h^s = 0$. The dotted curves delineate regions of the MPPN self-assembly diagram dominated by distinct MPPN n states, while the solid lines show the corresponding estimates obtained from Eq. (C2). The red horizontal lines are obtained as in Fig. 4. The small-α boundaries of the red horizontal lines are used to fix $\mathscr{C}$ in Eq. (C2) for each n considered. We use the same notation as in Fig. 2.

by this particular MPPN n state. Figure 11 suggests that, for small-enough r^s, Eq. (C2) provides a good estimate of the boundaries separating regions of MPPN self-assembly diagrams dominated by distinct MPPN n states. We find, however, that these boundaries intersect at large-enough r^s (see also Fig. 4). Equation (C2) does not apply in this regime. We also note that, if h^s is increased to a finite value, larger r^s are required for protein domains outside the membrane to shift MPPN self-assembly diagrams, which further limits the applicability of Eq. (C2).

[1] R. Phillips, J. Kondev, J. Theriot, and H. Garcia, *Physical Biology of the Cell* (Garland Science, New York, 2012).

[2] B. Alberts, A. D. Johnson, J. Lewis, D. Morgan, M. Raff, K. Roberts, and P. Walte, *Molecular Biology of the Cell* (Garland Science, New York, 2015).

[3] D. M. Engelman, Membranes are more mosaic than fluid, Nature **438**, 578 (2005).

[4] D. H. Boal, *Mechanics of the Cell* (Cambridge University Press, Cambridge, UK, 2012).

[5] R. Phillips, T. Ursell, P. Wiggins, and P. Sens, Emerging roles for lipids in shaping membrane-protein function, Nature **459**, 379 (2009).

[6] T. Basta, H. J. Wu, M. K. Morphew, J. Lee, N. Ghosh, J. Lai, J. M. Heumann, K. Wang, Y. C. Lee, D. C. Rees, and M. H. B. Stowell, Self-assembled lipid and membrane protein polyhedral nanoparticles, Proc. Natl. Acad. Sci. USA **111**, 670 (2014).

[7] H.-J. Wu, T. Basta, M. Morphew, D. C. Rees, M. H. B. Stowell, and Y. C. Lee, Microfluidic device for super-fast evaluation of membrane protein crystallization, In *Proceedings of the 8th Annual IEEE International Conference on Nano/Micro Engineered and Molecular Systems* (IEEE, Los Alamitos, CA, 2013), pp. 84–87.

[8] W. Zhang, P. R. Chipman, J. Corver, P. R. Johnson, Y. Zhang, S. Mukhopadhyay, T. S. Baker, J. H. Strauss, M. G. Rossmann, and R. J. Kuhn, Visualization of membrane protein domains by cryo-electron microscopy of dengue virus, Nat. Struct. Mol. Biol. **10**, 907 (2003).

[9] Z. Liu, H. Yan, K. Wang, T. Kuang, J. Zhang, L. Gui, X. An, and W. Chang, Crystal structure of spinach major light-harvesting complex at 2.72 a resolution, Nature **428**, 287 (2004).

[10] J. J. B. Cockburn, N. G. A. Abrescia, J. M. Grimes, G. C. Sutton, J. M. Diprose, J. M. Benevides, G. J. Thomas, J. K. H. Bamford, D. H. Bamford, and D. I. Stuart, Membrane structure and interactions with protein and dna in bacteriophage prd1, Nature **432**, 122 (2004).

[11] D. Li, O. Kahraman, and C. A. Haselwandter, Symmetry and size of membrane protein polyhedral nanoparticles, Phys. Rev. Lett. **117**, 138103 (2016).

[12] D. Li, O. Kahraman, and C. A. Haselwandter, Controlling the shape of membrane protein polyhedra, Europhys. Lett. **117**, 58001 (2017).

[13] R. MacKinnon, Potassium channels and the atomic basis of selective ion conduction, Biosci. Rep. **24**, 75 (2004).

[14] S. Takamori, M. Holt, K. Stenius, E. A. Lemke, M. Grønborg, D. Riedel, H. Urlaub, S. Schenck, B. Brügger, P. Ringler, S. A. Müller, B. Rammner, F. Gräter, J. S. Hub, B. L. De Groot, G. Mieskes, Y. Moriyama, J. Klingauf, H. Grubmüller, J. Heuser, and F. Wieland, Molecular anatomy of a trafficking organelle, Cell **127**, 831 (2006).

[15] K. R. Vinothkumar and R. Henderson, Structures of membrane proteins, Quart. Rev. Biophys. **43**, 65 (2010).

[16] L. A. Sazanov, A giant molecular proton pump: Structure and mechanism of respiratory complex I, Nat. Rev. Mol. Cell Biol. **16**, 375 (2015).

[17] F. Li, Structure, function, and evolution of coronavirus spike proteins, Ann. Rev. Virol. **3**, 237 (2016).

[18] D. Wrapp, N. Wang, K. S. Corbett, J. A. Goldsmith, C.-L. Hsieh, O. Abiona, B. S. Graham, and J. S. McLellan, Cryo-EM structure of the 2019-nCoV spike in the prefusion conformation, Science **367**, 1260 (2020).

[19] A. C. Walls, Y.-J. Park, M. A. Tortorici, A. Wall, A. T. McGuire, and D. Veesler, Structure, function, and antigenicity of the SARS-CoV-2 spike glycoprotein, Cell **181**, 281 (2020).

[20] M. Ma, D. Li, O. Kahraman, and C. A. Haselwandter, Symmetry of membrane protein polyhedra with heterogeneous protein size, Phys. Rev. E **101**, 022417 (2020).

[21] A. Ben-Shaul and W. M. Gelbart, Statistical thermodynamics of amphiphile self-assembly: Structure and phase transitions in micellar solutions, in *Micelles, Membranes, Microemulsions, and Monolayers* (Springer, New York, 1994), pp. 1–104.

[22] S. A. Safran, *Statistical Thermodynamics of Surfaces, Interfaces, and Membranes* (Westview Press, Boulder, CO, 2003).

[23] R. F. Bruinsma, W. M. Gelbart, D. Reguera, J. Rudnick, and R. Zandi, Viral Self-Assembly as a Thermodynamic Process, Phys. Rev. Lett. **90**, 248101 (2003).

[24] M. Ø. Jensen and O. G. Mouritsen, Lipids do influence protein function-the hydrophobic matching hypothesis revisited, Biochim. Biophys. Acta **1666**, 205 (2004).

[25] O. S. Andersen and R. E. Koeppe, Bilayer thickness and membrane protein function: An energetic perspective, Annu. Rev. Biophys. Biomol. Struct. **36**, 107 (2007).

[26] T. R. Weikl, Membrane-mediated cooperativity of proteins, Ann. Rev. Phys. Chem. **69**, 521 (2018).

[27] R. B. Bass, P. Strop, M. Barclay, and D. C. Rees, Crystal structure of *Escherichia coli* MscS, a voltage-modulated and mechanosensitive channel, Science **298**, 1582 (2002).

[28] S. Steinbacher, R. B. Bass, P. Strop, and D. C. Rees, *Structures of the Prokaryotic Mechanosensitive Channels MscL and MscS*, volume 58 of Current Topics in Membranes (Academic Press, New York, 2007).

[29] W. T. Góźdź and G. Gompper, Shape transformations of two-component membranes under weak tension, Europhys. Lett. **55**, 587 (2001).

[30] T. Auth and G. Gompper, Budding and vesiculation induced by conical membrane inclusions, Phys. Rev. E **80**, 031901 (2009).

[31] M. M. Müller and M. Deserno, Cell model approach to membrane mediated protein interactions, Prog. Theor. Phys. Supp. **184**, 351 (2010).

[32] N. Dan, A. Berman, P. Pincus, and S. A. Safran, Membrane-induced interactions between inclusions, J. Phys. II France **4**, 1713 (1994).

[33] J.-B. Fournier, Microscopic membrane elasticity and interactions among membrane inclusions: interplay between the shape, dilation, tilt and tilt-difference modes, Eur. Phys. J. B Condens. Matter Compl. Syst. **11**, 261 (1999).

[34] S. Weitz and N. Destainville, Attractive asymmetric inclusions in elastic membranes under tension: Cluster phases and membrane invaginations, Soft Matter **9**, 7804 (2013).

[35] O. Kahraman, P. D. Koch, W. S. Klug, and C. A. Haselwandter, Architecture and function of mechanosensitive membrane protein lattices, Sci. Rep. **6**, 19214 (2016).

[36] P. B. Canham, The minimum energy of bending as a possible explanation of the biconcave shape of the human red blood cell, J. Theor. Biol. **26**, 61 (1970).

[37] W. Helfrich, Elastic properties of lipid bilayers: Theory and possible experiments, Z. Naturforsch. C **28**, 693 (1973).

[38] E. A. Evans, Bending resistance and chemically induced moments in membrane bilayers, Biophys. J. **14**, 923 (1974).

[39] W. Rawicz, K. C. Olbrich, T. McIntosh, D. Needham, and E. Evans, Effect of chain length and unsaturation on elasticity of lipid bilayers, Biophys. J. **79**, 328 (2000).

[40] B. van Brunt, *The Calculus of Variations* (Springer-Verlag, New York, 2004).

[41] T. Ursell, J. Kondev, D. Reeves, P. A. Wiggins, and R. Phillips, The role of lipid bilayer mechanics in mechanosensation, in *Mechanosensitivity in Cells and Tissues 1: Mechanosensitive Ion Channels*, edited by A. Kamkin and I. Kiseleva (Springer, New York, 2008), pp. 37–70.

[42] H. W. Huang, Deformation free energy of bilayer membrane and its effect on gramicidin channel lifetime, Biophys. J. **50**, 1061 (1986).

[43] P. Wiggins and R. Phillips, Membrane-protein interactions in mechanosensitive channels, Biophys. J. **88**, 880 (2005).

[44] C. Nielsen, M. Goulian, and O. S. Andersen, Energetics of inclusion-induced bilayer deformations, Biophys. J. **74**, 1966 (1998).

[45] B. W. Clare and D. L. Kepert, The closest packing of equal circles on a sphere, Proc. R. Soc. Lond. A **405**, 329 (1986).

[46] B. W. Clare and D. L. Kepert, The optimal packing of circles on a sphere, J. Math. Chem. **6**, 325 (1991).

[47] Y. Kantor, M. Kardar, and D. R. Nelson, Tethered surfaces: Statics and dynamics, Phys. Rev. A **35**, 3056 (1987).

[48] K. V. Damodaran and K. M. Merz, Head group-water interactions in lipid bilayers: A comparison between DMPC- and DLPE-based lipid bilayers, Langmuir **9**, 1179 (1993).

[49] G. W. Hart, The encyclopedia of polyhedra (2000) [https://www.georgehart.com/virtual-polyhedra/vp.html].

[50] S. Li, P. Roy, A. Travesset, and R. Zandi, Why large icosahedral viruses need scaffolding proteins, Proc. Natl. Acad. Sci. USA **115**, 10971 (2018).

[51] S. Panahandeh, S. Li, and R. Zandi, The equilibrium structure of self-assembled protein nano-cages, Nanoscale **10**, 22802 (2018).

[52] E. Perozo, A. Kloda, D. Marien Cortes, and B. Martinac, Physical principles underlying the transduction of bilayer deformation forces during mechanosensitive channel gating, Nat. Struct. Biol. **9**, 696 (2002).

[53] R. R. Draheim, A. F. Bormans, R.-Z. Lai, and M. D. Manson, Tuning a bacterial chemoreceptor with protein-membrane interactions, Biochemistry **45**, 14655 (2006).

[54] M. Howarth, K. Takao, Y. Hayashi, and A. Y. Ting, Targeting quantum dots to surface proteins in living cells with biotin ligase, Proc. Natl. Acad. Sci. USA **102**, 7583 (2005).